Journal of Nanobiotechnology

RESEARCH

Open Access

In vivo fluorescence imaging of nanocarriers in near-infrared window II based on aggregation-caused quenching

Zichen Zhang[1], Chang Liu[1], Yi Lu[1,2,4], Weili Zhao[1,2], Quangang Zhu[2], Haisheng He[1*], Zhongjian Chen[2*] and Wei Wu[1,2,3,4*]

Abstract

Accurate fluorescence imaging of nanocarriers in vivo remains a challenge owing to interference derived mainly from biological tissues and free probes. To address both issues, the current study explored fluorophores in the near-infrared (NIR)-II window with aggregation-caused quenching (ACQ) properties to improve imaging accuracy. Candidate fluorophores with NIR-II emission, ACQ984 (λ_{em} = 984 nm) and IR-1060 (λ_{em} = 1060 nm), from the aza-BODIPY and cyanine families, respectively, were compared with the commercial fluorophore ICG with NIR-II tail emission and the NIR-I fluorophore P2 from the aza-BODIPY family. ACQ984 demonstrates high water sensitivity with complete fluorescence quenching at a water fraction greater than 50%. Physically embedding the fluorophores illuminates various nanocarriers, while free fluorophores cause negligible interference owing to the ACQ effect. Imaging based on ACQ984 revealed fine structures in the vascular system at high resolution. Moreover, good in vivo and ex vivo correlations in the monitoring of blood nanocarriers can be established, enabling real-time noninvasive in situ investigation of blood pharmacokinetics and dynamic distribution in various tissues. IR-1060 also has a good ACQ effect, but the lack of sufficient photostability and steady post-labeling fluorescence undermines its potential for nanocarrier bioimaging. P2 has an excellent ACQ effect, but its NIR-I emission only provides nondiscriminative ambiguous images. The failure of the non-ACQ probe ICG to display the biodistribution details serves as counterevidence for the improved imaging accuracy by NIR-II ACQ probes. Taken together, it is concluded that fluorescence imaging of nanocarriers based on NIR-II ACQ probes enables accurate in vivo bioimaging and real-time in situ pharmacokinetic analysis.

Keywords Nanocarriers, Fluorescence imaging, Near-infrared II, Aggregation-caused quenching, Aza-BODIPY, In situ pharmacokinetics

*Correspondence:
Haisheng He
he_haisheng@fudan.edu.cn
Zhongjian Chen
aajian818@163.com
Wei Wu
wuwei@shmu.edu.cn

[1]School of Pharmacy, Fudan University, Key Laboratory of Smart Drug Delivery, Ministry of Education, Shanghai 201203, China
[2]Shanghai Skin Disease Hospital, Tongji University School of Medicine, Shanghai 200443, China
[3]Center for Medical Research and Innovation, Shanghai Pudong Hospital, Fudan University Pudong Medical Center, Shanghai 201399, China
[4]Fudan Zhangjiang Institute, Shanghai 201203, China

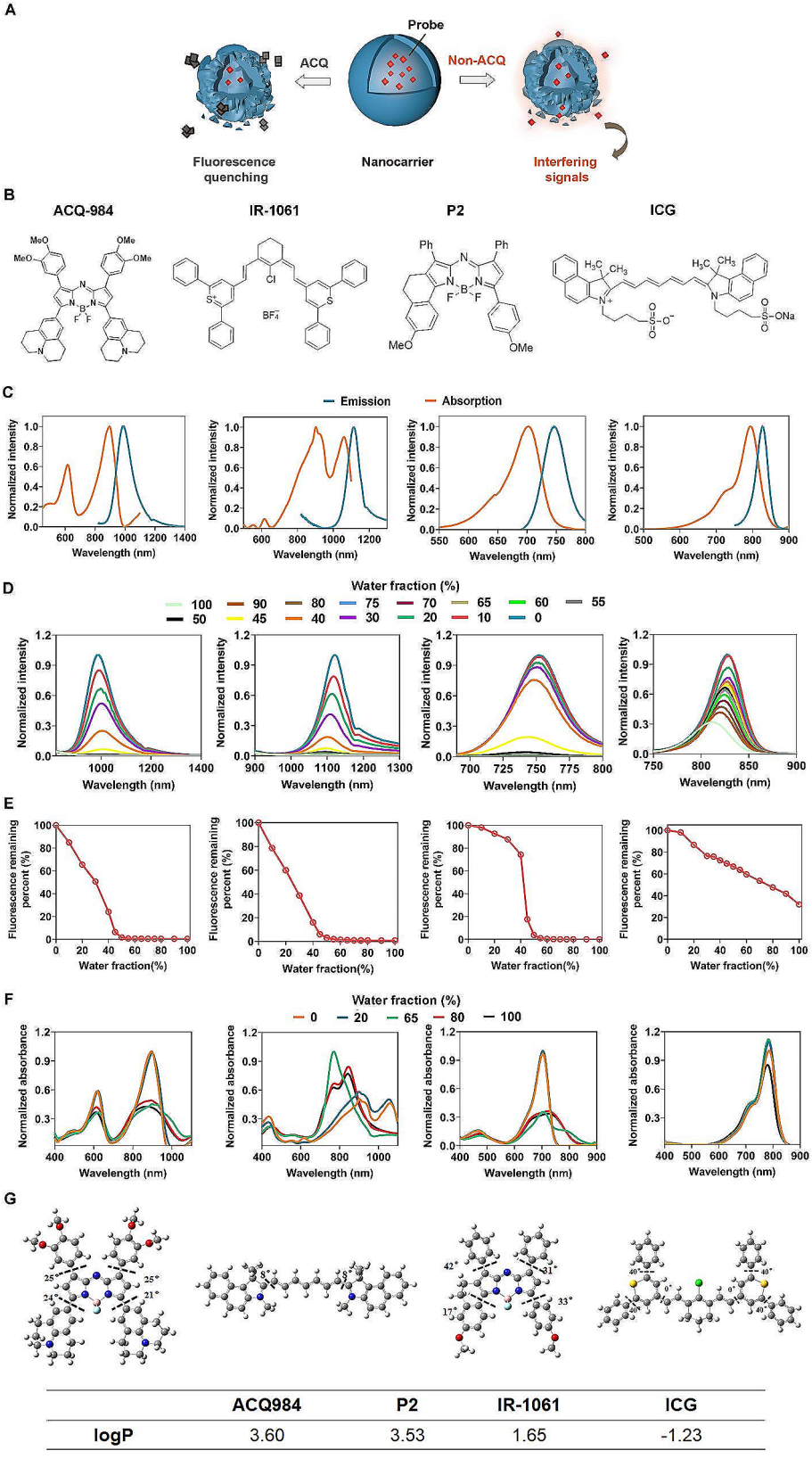

	ACQ984	P2	IR-1061	ICG
logP	3.60	3.53	1.65	-1.23

Fig. 1 (See legend on next page.)

(See figure on previous page.)

Fig. 1 Spectroscopic properties and ACQ effect of selected probes. (**A**) Schematic illustration of the differences between ACQ and non-ACQ probes for fluorescence imaging of nanocarriers. (**B**) Chemical structures of ACQ984, IR-1061, P2, and ICG. (**C**) Normalized absorption and emission spectra of the four probes dissolved in DMSO. (**D**) Fluorescence spectra of selected probes as a function of the water fraction in the binary DMSO/water system. (**E**) Fluorescence intensity vs. water fraction curves that identify the starting point of absolute fluorescence quenching. (**F**) UV spectra of selected probes in the binary DMSO/water system as a function of the water fraction. (**G**) Molecular optimization, dihedral angle calculation, and logP values of four selected probes. The sequence in plots of (**C**), (**D**), (**E**), (**F**) and (**G**) correspond to the sequence of the fluorophores ACQ984, IR-1061, P2, and ICG, whose chemical structures are displayed in (**B**)

Introduction

Advances in drug delivery have renovated clinical pharmacotherapy and the pharmaceutical industry in recent decades. To protect drug payloads, transport them to target sites, and release them in a controlled way, carriers, especially nanocarriers, are often used for drug delivery. Recent years have witnessed enthusiastic research input and rapid progress in nanocarrier drug delivery systems (NDDSs) [1, 2]. However, the translation of NDDSs is not as successful as expected despite several tens of NDDS products being officially approved [3, 4]. The ignorance of in vivo behaviors is believed to be one of the leading causes of the translation gap [4, 5]. Unveiling the in vivo fate and underlying mechanisms facilitates preclinical optimization and accelerates the translation of NDDSs [4, 6, 7].

Tracking and imaging of nanocarriers play an indispensable role in the exploration of the in vivo behaviors of nanocarriers. Among the various imaging tools available, fluorescence imaging is more sensitive, more accessible, and easier to implement. Recent years have seen growing applications of fluorescence imaging in drug delivery. For instance, it has become routine to validate the biodistribution and targeted delivery of drug nanocarriers due to the implementation of small-animal in vivo illumination systems (IVIS) based on fluorescence imaging in the near-infrared (NIR) region [8–10]. However, the accuracy of fluorescence imaging is being challenged because of the accumulation of deceptive readouts [11–14].

The most remarkable challenge with fluorescence imaging of nanocarriers (FIN) lies in the inherent drawbacks of fluorescence imaging, i.e., limited penetration depth due to tissue absorption and diffraction as well as interference derived from tissue autofluorescence. Fortunately, these drawbacks could be greatly mitigated at longer emission wavelengths. Recently, fluorescence in the NIR-II (1000–1700 nm) region has been successfully applied in bioimaging [8, 15] but has not been purposely applied for FIN. The implementation of NIR-II fluorophores for tracking and imaging nanocarriers in vivo is highly desirable. Another leading challenge in FIN is the discrimination of vehicle-bound signals from free-probe signals [4, 12, 16, 17]. Analysis of nanocarriers requires the establishment of a robust correlation between fluorescence and drug nanocarriers. If the fluorophores are secured with vehicles, the signals can be reliably employed to represent the nanocarriers, and there is not much concern about non-nanocarrier signals [12]. Nevertheless, if nonencapsulated or released fluorophores coexist, which is common because drug nanocarriers are generally designed to be biodegradable for safety considerations, unbound signals may generate a certain degree of interference (Fig. 1A) [12, 17]. How to preclude this kind of interference remains one of the leading issues in FIN.

In recent years, the application of environment-responsive probes based on the rationale of Förster resonance energy transfer (FRET) has made progress toward the identification of nanocarrier integrity [18–20]. FRET occurs when a pair of donors/acceptors, such as Cy5.5/Cy5 and DiI/DiD, are spatially adjacent (e.g., when embedded in nanocarriers), normally less than 10 nm in distance [20, 21]. Disintegration or degradation severs the FRET pair and leads to signal switching, based on which the structural integrity of nanocarriers can be estimated [21–23]. However, as FRET runs by an "on-to-on" mechanism and involves at least two fluorophores, it is difficult to discriminate nanocarriers from interfering signals owing to complicated factors such as individual illumination and non-FRET-specific excitation [24, 25]. The accuracy of FRET-based bioimaging still awaits validation [26, 27]. In addition to FRET, other ratiometric fluorescence imaging strategies also invove two, or occasionally more, fluorophores and therefore encounter problems similar to FRET [28]. Fluorophores based on aggregation-induced emission (AIE) can illuminate nanocarriers when physically embedded due to "restriction of intramolecular motion" and have been utilized for bioimaging of different types of nanoparticles [29, 30]. However, the tendency of free or released AIE molecules to form aggregates and induce emission may cause a certain degree of interference with the nanocarrier signals, which is very difficult to eliminate [29, 30]. Many other environment-responsive probes only respond to one or a limited number of environmental factors, such as pH or specific biomarkers, rendering them less flexible and unreliable to work as a universal tool for FIN [31].

To address the dual challenges of FIN, we used an alternative strategy by eliminating the interference caused by free probes and extending the imaging wavelengths to the NIR-II window simultaneously. It is hypothesized that absolute quenching of free or released probes would function to preclude interfering fluorescence (Fig. 1A). It is generally recognized that a series of fluorophores

are able to demonstrate an aggregation-caused quenching (ACQ) effect [17, 32–37], a common phenomenon in which fluorophores of a certain degree of hydrophobicity and molecular planarity tend to aggregate in an aqueous environment with simultaneous fluorescence quenching [17, 38]. ACQ is always regarded as adverse in bioimaging but functions well as a tool for FIN [17]. Fluorophores with ACQ properties illuminate nanocarriers when embedded and dispersed in a molecular state, whereas free or released fluorophores form aggregates spontaneously upon contact with water with fluorescence quenching to near zero [17, 32, 39]. Therefore, the observed fluorescence could be directly correlated with the nanocarriers. In this respect, ACQ outperforms FRET because it involves only one fluorophore and involves simpler "on-to-off" signal switching, which corresponds well to nanocarrier degradation. The complete quenching of the ACQ probe eliminates the interference caused by leaked free probes, conquering the drawbacks of imaging based on conventional non-ACQ probes. ACQ, as a common environment-responsive phenomenon, can achieve universal application for nanoparticle labeling. To date, the ACQ concept has only been explored for FIN in the NIR-I (700–900 nm) window [32–37, 40–42].

The current study aimed to identify NIR-II fluorophores with ACQ properties and test their applicability in FIN with improved accuracy. In the spectra of recently reported NIR-II fluorophores, some display a certain degree of ACQ. IR-1061, a probe belonging to the cyanine family, demonstrates spontaneous ACQ-like water sensitivity [43]. On the other hand, a group of aza-BODIPY-based fluorophores (e.g., NJ1060) that demonstrate maximum emissions in the NIR-II region [44] may also possess a potential ACQ effect based on our judgment of their hydrophobicity and planarity. Therefore, in this study, we tested the probable ACQ effect of selected fluorophores with NIR-II emission (Fig. 1B) and explored their potential for FIN in comparison with that of the frequently utilized NIR-I fluorophore P2 and the clinically available fluorophore indocyanine green (ICG) with NIR-II tail emission.

Materials and methods

The detailed materials and methods used are provided in the Supplementary Information.

Spectroscopic studies

All selected probes were dissolved in dimethyl sulfoxide (DMSO) before determination. The UV spectra were recorded by a UV−visible spectrophotometer. The fluorescence spectra and intensities were recorded by a fluorescence spectrophotometer. The excitation wavelengths for ACQ984, IR-1061, P2, and ICG were 808, 808, 650, and 700 nm, respectively.

ACQ effect of selected probes

All selected probes were first dissolved in DMSO and then added to either DMSO/water or acetonitrile (ACN)/water binary systems with a series of water fractions ranging from 1 to 99% at a volume ratio of 1:100 and a final molar concentration of 9.4 μM. The fluorescence of each sample was determined by a fluorescence spectrophotometer. Plots of fluorescence intensity vs. water fraction were generated to pinpoint the onset of aggregation and complete fluorescence quenching.

Evaluation of fluorescence reillumination

The DMSO solutions of selected probes were added directly to PBS to allow the probes aggregate and quench completely. Then, the quenched probes were immediately transferred to PBS, rat plasma, and 1% Tween 80 and incubated at 37 °C for 24 h to evaluate fluorescence reillumination. To simulate the probe release process more closely, probes dissolved in DMSO were directly added to different media and incubated at 37 °C for 24 h.

To evaluate fluorescence reillumination in vivo, the probes were prequenched following the same procedures as for the in vitro study except that the water was replaced with 0.9% NaCl solution. The prequenched probe dispersions (200 μL) were then injected into each nude mouse *via* the tail vein and imaged by an IVIS imaging system at selected time points.

Preparation and labeling of various nanocarriers

PMs were prepared by a thin-film hydration method. $mPEG_{2k}$-$PDLLA_{2k}$ was loaded with P2, ICG, IR-1061 or ACQ984 at mass ratios of 1000:1, 2500:1, 800:1 or 400:1. PCL and PEG-PCL nanoparticles were prepared by an emulsification/solvent evaporation method. PCL nanoparticles were loaded with P2, IR-1061 or ACQ984 at mass ratios of 2000:1, 450:1 or 340:1. PEG-PCL nanoparticles were prepared by the same method except for the addition of 29% (w/w) $mPEG_{5k}$-PCL_{45k} to PCL.

The morphology of the nanocarriers was observed via transmission electron microscopy (TEM). The hydrodynamic size and zeta potential of the different nanocarriers were characterized by a nanosizer. The fluorescence spectra of the different formulations were recorded by a fluorospectrophotometer, and the corresponding fluorescence images were visualized by an IVIS imaging system. Fluorescence stability was evaluated in 0.01 M PBS (pH 7.4) and plasma by an IVIS imaging system. The encapsulation efficiency (EE%) of ACQ984-PMs was measured by ultrafiltration. EE% was calculated as the remaining percentage of fluorescence intensity in the ultrafiltration centrifuge tube. The EE % of the ICG-PMs was measured following the same procedures except that the fluorescence measurements were replaced by ultraviolet absorption measurements. ICG leakage was also measured by

ultrafiltration, and the ultraviolet absorption of the filtrate was measured to calculate the amount of released ICG.

Optical penetration study in tissue phantom

Optical tissue penetration was investigated utilizing 1% Intralipid® as an imitating tissue because of their similar scattering properties. Capillaries filled with PM dispersion were immersed in 1% Intralipid® at different depths and then imaged by an IVIS imaging system (PerkinElmer, UK) and a NIRvana SWIR camera (Princeton Instruments Inc.). The scattering effect was calculated as the ratio of the full width at half-maximum (FWHM) to the measured width of the capillary, which was expressed as follows: Scattering effect = $\text{pixel}_{\text{FWHM}}/\text{pixel}_{\text{capillary width}}$.

The fluorescence intensity of each image was set to a similar value.

In vivo imaging of blood and lymphatic vessels

PM dispersions (0.2 mL) were intravenously injected into nude mice. For ACQ984-PMs and IR1061-PMs, the mean fluorescence intensity (under the same optical conditions) before injection was adjusted to the same value. The fluorescence intensity (FI) profiles across the marked (red) line of interest were plotted. For the SNR calculation, the background noise area was selected from positions 0-0.2 and 0.8-1.0 (normalized position), and the average fluorescence intensity was calculated as the background signal. The SNR of the liver region was calculated by the mean fluorescence intensity (MFI) ratio between the liver and the blank area below. The calculation is briefly expressed as follows:

$\text{SNR}_{\text{vessel}} = \text{Maximum FI}/\text{Average FI}_{\text{position: 0–0.2 and 0.8–1.0}}$.
$\text{SNR}_{\text{liver}} = \text{mean FI}_{\text{liver}}/\text{mean FI}_{\text{blank area below}}$.

Vascular and main organ imaging for in vivo–ex vivo correlation

Male nude mice (20 g) were purchased from Shanghai Laboratory Animal Center (Shanghai, China). For long-term imaging, animals were anesthetized by intraperitoneal injection of tribromoethanol (Avertin, 1.25%, 0.4 mL), while for temporary imaging, animals were anesthetized by isoflurane.

A small animal IVIS system (PerkinElmer) was used for NIR-I bioimaging. For NIR-II bioimaging, a custom-built imaging setup integrating an InGaAs SWIR camera (NIRvana 640, Princeton Instruments, US; 640×512 pixel), a camera lens (SWIR-35, Navitar) and various emission filters (ThorLabs) was used. An external 808 nm diode laser (MDL-N-808–10 W BJ00373, Changchun New Industries Optoelectronics Tech. Co., Ltd.) coupled into a 450-μm core metal-cladded multimode fiber was selected for excitation. The InGaAs camera was cooled to −80 °C, and different exposure times were used to allow sufficient signal. All images were background corrected within the LightField imaging software and processed with ImageJ (Fiji).

The experimental data are presented as the means ± standard deviations. The statistical significance of differences between the control and experimental groups was analyzed by *t* test or one-way ANOVA utilizing GraphPad Prism 8. The full width at half-maximum (FWHM), correlation coefficient and linear fit were analyzed by Origin 64. All images were manipulated by ImageJ. The mean fluorescence intensity of in vivo blood vessels was automatically calculated by ImageJ-macro. Related PK parameters were calculated by DAS 2.0.

Results and discussion

Spectroscopic properties and the ACQ effect

ACQ984 is a newly synthesized probe with an aza-BODIPY parent structure that resembles that of NJ1060 [44]. The synthetic procedures and structural identification data are provided in the Supplementary Information. The chemical structures and fluorescence spectra of all selected probes are presented in Fig. 1B&C. ACQ984 showed maximum excitation (λ_{ex}) and emission (λ_{em}) at 873 nm and 984 nm, respectively, in DMSO (Fig. 1C). The photophysical parameters of all selected probes are presented in Table S1. The quantum yields of ACQ984 at 850–1500 nm and 1000–1500 nm were 3.09% and 0.43%, respectively. Its quantum yield is higher than that of marketed IR-1061 under maximum emission wavelengths and comparable under longer imaging wavelengths (>1000 nm). Although ICG has the highest quantum yield, its water solubility limits its ACQ effect. Compared to our previously synthesized BODIPY-structured probe P2, the quantum yield of ACQ984 significantly increased. In contrast to IR-1061 and ICG, whose fluorescence is attenuated after continuous excitation, two aza-BODIPY-structured probes, ACQ984 and P2, show superior photostability (Fig. S1D).

The ACQ effect of the selected fluorophores was validated by observing fluorescence quenching as a function of the water fraction in a binary DMSO/water system [32, 38, 39]. The fluorescence of all four probes decreased with a slight wavelength shift in response to the increase in water content (Fig. 1D). ACQ984 is completely quenched at a water fraction less than that of P2 (50% vs. 55%), indicating a higher water sensitivity or a better ACQ effect (Fig. 1E) [38]. With the same parent structure, both display similar absorption spectra with a slight redshift and peak broadening at a water fraction above 20% (Fig. 1F), which is indicative of the formation of J-aggregates [32, 45]. IR-1061 was also completely quenched when the water fraction increased to 60% or more (Fig. 1E). The emergence of blueshifted peaks between 700 and 900 nm

and intensified absorption in response to the increase in the water fraction suggest the formation of H-aggregates (Fig. 1F) [46, 47]. ICG, a hydrophilic probe, also exhibits a certain degree of water sensitivity, but its fluorescence remains at 30% of its original value in pure water (Fig. 1E). The absorption spectra were not indicative of the formation of either H- or J-aggregates (Fig. 1F). The decreased fluorescence and absorption may result from concentration-caused quenching [48]. The ACQ effect was further confirmed in an ACN/water binary system (Fig. S1A-C) for all selected probes. The similar performance in different solvent systems underlines the determining role of water, rather than the solvent environment, in their aggregation behaviors.

The exploration of NIR-II fluorophores with ACQ properties was also expanded to include the DAD-structured probe IR-FTE analog [49] and another commercially available cyanine fluorophore, IR-26 (Fig. S2A). Both probes are sensitive to water, showing a gradual decrease in fluorescence with increasing water content in both the ACN/water and DMSO/water binary systems (Fig. S2). However, the IR-FTE analog cannot quench completely in pure water, with 15% fluorescence remaining (Fig. S2B&C). IR-26 only displays complete fluorescence quenching at a relatively high water fraction above 75–80% in the ACN binary system and shows very different quenching behaviors in different solvent systems (Fig. S2D&E), which implies high variation when utilizing this probe to label nanocarriers. Taken together, these preliminary spectroscopic data suggest the potential utility of these materials as NIR-II ACQ probes.

Theoretical calculations using a B3LYP/6–31 + G (d, p) basis set were utilized to examine the geometric properties of the selected fluorophores. Considering the low contribution of alkyl moieties to the geometric properties of ICG, those chains were removed to reduce the complexity of the theoretical calculations. As shown in Fig. 1G, the P2 molecule indicates good planarity with peripheral phenyl rings at a slight dihedral angle with the aza-BODIPY core, which is consistent with its superior ACQ properties. Compared with that of P2, the dihedral angle between the 1-, 5-, and 7-phenyl rings and the aza-BODIPY core was lower in the ACQ984 molecule, indicating increased planarity, which may have contributed to the enhanced conjugation of the ACQ984 moieties from 4-methoxybenzene or julolidine moieties to the aza-BODIPY core. The slight increase in torsion between julolidine at the 3-position and the aza-BODIPY core is ascribed to the absence of the constraint of ethylene in P2. IR-1061 also shows superior planarity, which corresponds to its high water sensitivity. LogP is another important parameter that influences the ACQ effect (Fig. 1G). Although the ICG core exhibits excellent planarity, which favors the ACQ effect, the hydrophilic chains render it water soluble, hampering the formation of aggregates. Similarly, ACQ984, which has the highest logP value, has the greatest hydrophobicity, which indicates its high water sensitivity.

Fluorescence reillumination

Another important characteristic of ACQ probes is the stability of the quenched states. Ideally, quenched probes should maintain a complete quenching state for an extended time. Otherwise, any fluctuation in the quenched state may lead to a biased readout. Unfortunately, quenched probe aggregates tend to repartition into hydrophobic domains such as membrane structures and protein pockets in complex biomedia and can be reilluminated to create artifacts if their cohesion is less than that between the probe molecules and the docking domains. Instantaneous quenching and maintenance of a stable quenched state with minimal reillumination are key factors for ensuring imaging reliability.

ICG was excluded for evaluating reillumination because it was not quenched in water first. As illustrated in Fig. 2A, all probes quench immediately upon dispersion in plasma. The remaining fluorescence for ACQ984 was only 0.5%, whereas it was approximately 1% for P2 (Fig. 2A). After the addition of prequenched probes to plasma, P2 had the highest reillumination of approximately 4.5% after 24 h of incubation at 37 °C, while ACQ984 and IR-1061 showed negligible fluorescence reillumination of less than 1% (Fig. 2B).

Probe prequenching is an ideal model to simulate the processes of liberation of probes from nanocarriers and subsequent aggregation and quenching. In fact, a small fraction of probes may evade these processes and be directly transferred to hydrophobic constructs. To simulate this situation, probes dissolved in DMSO were added directly to plasma (1:100). After 24 h of incubation, P2 retained 20.28% of its original fluorescence (Fig. 2B). Under such extreme conditions, ACQ984 still showed little fluorescence reillumination (~4.3%) and superior quenching stability (Fig. 2B). IR-1061 showed the lowest fluorescence transfer of approximately 0.13% (Fig. 2B). The quenching stability of the selected probes in PBS and surfactant was also tested (Fig. S3). Compared to P2, ACQ984 shows comparable stable quenching in PBS but less fluorescence reillumination in 1% Tween 80. The much greater reillumination in 1% Tween 80 than in plasma indicates that fluorescence reillumination could be very high if there is enough opportunity for the probes to partition into the hydrophobic constructs. Reducing reillumination represents one of the future goals in molecular optimization. IR-1061 consistently underwent the least amount of reillumination.

In vivo fluorescence reillumination was further evaluated to highlight the advantages of the newly synthesized

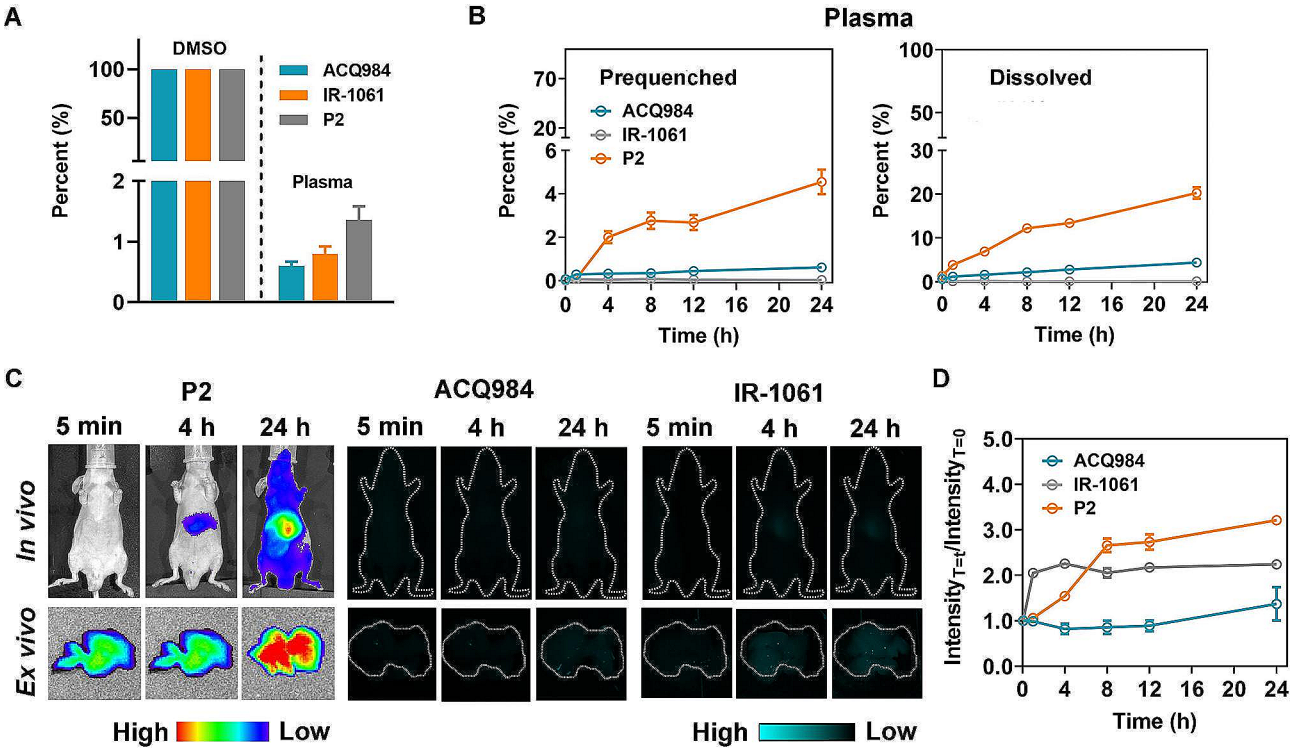

Fig. 2 Fluorescence quenching stability and reillumination of selected ACQ probes. (**A**) Fast fluorescence quenching of ACQ984, IR-1061, and P2 in rat plasma ($n=3$). The probes were dissolved in DMSO and added to rat plasma at a volume ratio of 1:100. The fluorescence intensity of the probes dissolved in DMSO at the same strength was set to 100%. (**B**) Reillumination of selected ACQ probes in plasma after 24 h of incubation ($n=3$). Probe solutions were added to plasma in the prequenched state or dissolved state (in DMSO). (**C**) Fluorescence reillumination of selected ACQ probes in vivo and ex vivo. (**D**) Fluorescence reillumination in the liver ($n=3$), which was calculated as the ratio of hepatic fluorescence intensity to hepatic autofluorescence before injection

NIR-II probe ACQ984. After injecting the prequenched probe dispersion, reillumination occurs mainly in the liver (Fig. 2C). Live imaging by ACQ984 demonstrated two-fold less reillumination than did imaging by P2 (Fig. 2D). However, IR-1061, which was not as stable as that tested in vitro, showed two times greater reillumination in the first hour and remained unchanged after 24 h of incubation. The greater complexity of the in vivo environment may account for this phenomenon. Ex vivo imaging of the liver further validated the low reillumination of ACQ984 (Fig. 2C). Both in vivo and ex vivo results support the better quenching stability of ACQ984, implying better imaging reliability.

Reliability of NIR-II ACQ probes for FIN

To highlight the superiority of the effect of ACQ on FIN, in vivo imaging was performed following the use of a labeling model nanocarrier, methoxy poly(ethylene glycol)$_{2k}$-poly(D, L-lactic acid)$_{2k}$ (mPEG$_{2k}$-PDLLA$_{2k}$) polymeric micelles (PMs), with ACQ984 in comparison with the commercial probe ICG. ICG was chosen for comparison because of its NIR-II emission and non-ACQ properties.

Owing to its high hydrophobicity, ACQ984 can be loaded into PM with a high loading efficiency of 97.6%. Despite its good water solubility, ICG can still be efficiently embedded in PMs with a loading efficiency of approximately 87%. ICG-loaded PMs displayed intense fluorescence (Fig. S4A). Although a small fraction of the ICG probes leaked after dilution and incubation for 1 h, the fluorescence intensity of the ICG-PM generally remained stable after the next 24 h of incubation (Figure S4B). Dilution always causes the burst release of PM; as a soluble molecule, ICG leaks easily. ICG leakage seems to alleviate the concentration-induced quenching of ICG loaded in PMs because of the fluorescence enhancement observed after a one-hour incubation [50]. Compared to that of ACQ984, severe self-quenching limits the ability of ICG to label PMs.

The biodistribution vs. time profiles of ACQ984-PMs and ICG-PMs differed greatly (Fig. 3A). The integration of signals from regions of interest (ROIs) indicated sustained hepatic and blood retention of the PMs by ACQ984, which corresponds to the long-circulating effect of PEGylated PMs (Fig. 3B&C). However, the behaviors of ICG-PMs and ICG probes are somewhat similar, demonstrating high hepatic accumulation and

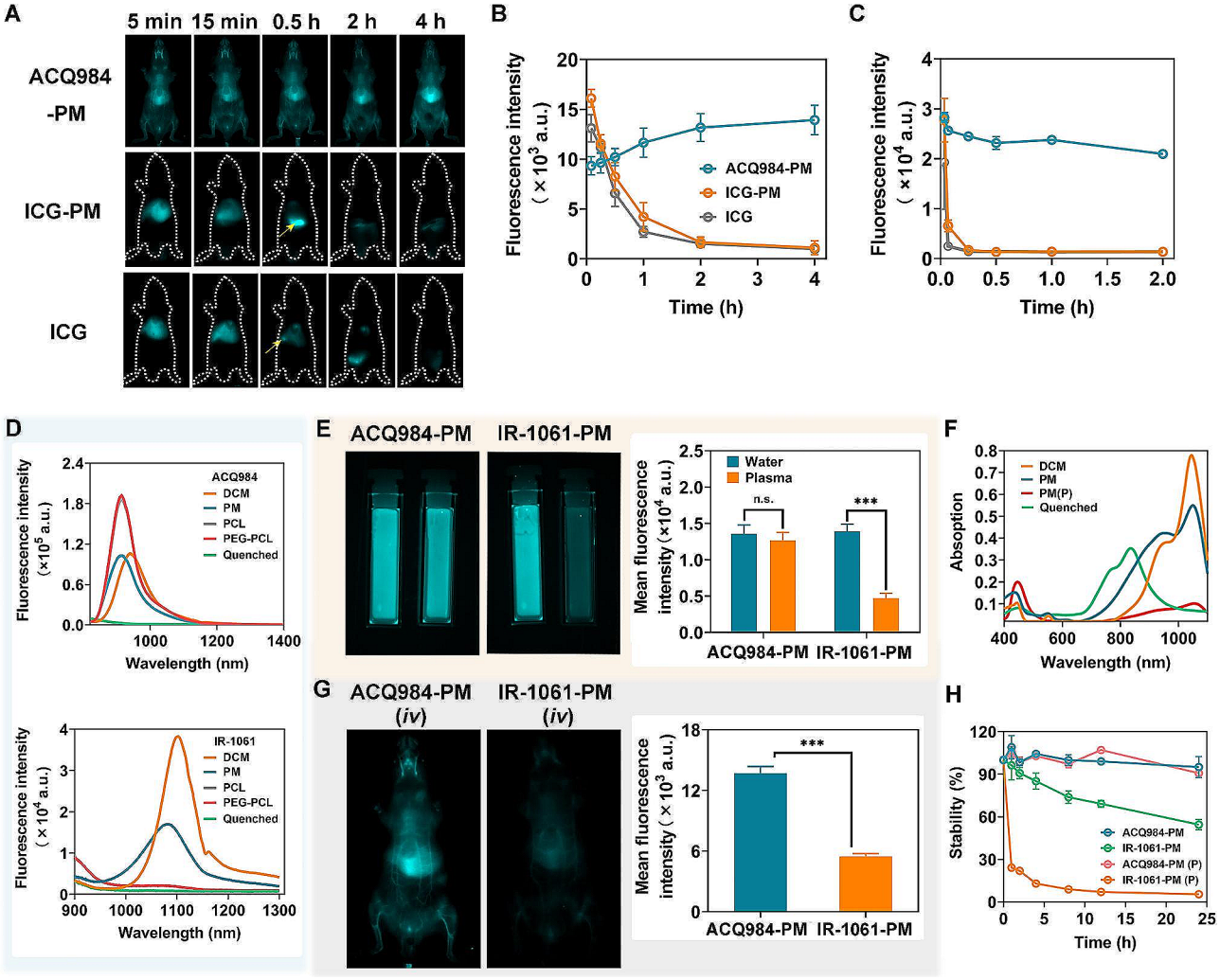

Fig. 3 Imaging reliability of the NIR-II ACQ probe. (**A**) In vivo live images following *iv* administration of ACQ984- and ICG-labeled PMs and free ICG. (The yellow arrow indicates the bile excretion of ICG or PM-ICG.) (**B**) Hepatic accumulation profiles ($n=3$) and (**C**) blood pharmacokinetic profiles ($n=3$) of ACQ984-PMs, ICG-PMs, and free ICG. (**D**) Fluorescence spectra of ACQ984 and IR-1061 dissolved in dichloromethane (DCM), loaded in nanocarriers, and quenched in water. (Fluorescence probes loaded in PCL and PEG-PCL show similar intensities, making the fluorescence curves highly coincident.) (**E**) Fluorescence images (left) and corresponding quantification (right) indicating the stability of ACQ984-PM and IR-1061-PM against dilution by water and plasma. (**F**) UV spectra of IR-1061 dissolved in DCM and quenched in water and IR1061-PM dispersed in water and plasma. The absorption of blank plasma was deducted before measurement. PM(P): PMs dispersed in plasma; PM: PMs dispersed in water. (**G**) Live images (left) and corresponding quantification (right) in nude mice following 5 min of *iv* administration through the tail vein of ACQ984-PM or IR1061-PM ($n=3$). (**H**) Fluorescence stability of the ACQ984-PM dispersion in PBS and plasma ($n=3$) after different incubation times. PM(P): PM dispersed in plasma; PM: PM dispersed in PBS. ***: $P<0.001$; n.s.: nonsignificant

rapid hepatic and blood elimination (Fig. 3B&C). The results demonstrated that ICG may have leaked in vivo. The signals observed are more likely derived from free probes and fail to represent the behaviors of the nanocarriers. This assumption is supported by the similar elimination pathways of the ICG-PM and free ICG groups, which are typically indicated by bile excretion beginning at 0.5 h (Fig. 3A, yellow arrow). The above findings prove that the wrong choice of probes may lead to disastrous readouts. Therefore, ICG was not further evaluated because of its inappropriate labeling ability demonstrated. The labeling capability of the selected ACQ probes was further tested for three kinds of nanocarriers with different structures or degrees of hydrophobicity, i.e., $mPEG_{2k}$-$PDLLA_{2k}$ PMs, polycaprolactone (PCL, Mn = 45,000) nanoparticles, and PEG-decorated PCL (PEG-PCL, with 29% $mPEG_{5k}$-PCL_{45k} adulterated) nanoparticles. TEM revealed a well-dispersed and spherical morphology. Both TEM and dynamic laser scattering analysis revealed a uniform particle distribution, and probe loading did not result in an apparent alteration in the particle size (Fig. S5A; Table S2). IR-1061 lost approximately 40% of its fluorescence when loaded in PMs, and the fluorescence of the PCL and PEG-PCL nanoparticles

was more significantly quenched (Fig. 3D). Although PCL-based materials have good affinity for IR-1061 [48], the handling procedures may have increased the opportunity for exposure to the water phases during preparation and led to premature quenching [43]. Belonging to the same aza-BODIPY family, ACQ984 shows a robust loading capacity similar to that of P2 irrespective of the type of nanocarrier (Fig. 3D). Higher illumination is achieved when ACQ984 is loaded in PCL or PEG-PCL nanoparticles, probably due to the greater core rigidity of these nanocarriers compared to that of PMs, which restricts probe mobility and reduces nonradiative decay [51]. Further challenging by plasma did not decrease the fluorescence stability of ACQ984-PMs, in contrast with the significant fluorescence loss and UV absorption disappearance observed for IR-1061-PMs (Fig. 3E&F). The UV spectrum also revealed a greater peak intensity at 950 nm for IR-1061 in the PMs (Fig. 3F), indicating the possible formation of lower quantum yield probe dimers in the PM cores [52], which accounted for the fluorescence loss of IR-1061 when loaded in the PMs. The dynamic equilibrium of PMs with their surroundings renders IR-1061-PMs more susceptible to fluorescence destabilization than more rigid nanoparticles, such as PCL and PEG-PCL nanoparticles (Fig. S5B-E) [43, 53, 54]. Probe leakage together with high sensitivity to environmental changes may account for these phenomena. The low fluorescence signal intensity of IR-1061-PMs in vivo further validated the low stability of IR-1061 labeling (Fig. 3G). Stable fluorescence was maintained in the nanocarriers after they were dispersed in PBS and plasma for up to 24 h for ACQ984, confirming the reliability of the representation of the intact nanocarriers by ACQ-based fluorescence (Fig. 3H&S5F). In contrast, IR-1061 gradually attenuated the fluorescence of nanocarriers dispersed in PBS, indicating continuous probe leakage or environment-induced quenching (Fig. 3H&S5F). This attenuation is aggravated by plasma components. All the above results support the use of ACQ984 as a potential NIR-II probe for FIN. IR-1061, which has extraordinarily high environmental sensitivity, is too fragile to be utilized to determine the integrity of nanocarriers, especially under physiological conditions.

ACQ984-based NIR-II imaging defines the ROI well

The accuracy of FIN depends strongly on the resolution of imaging, which in turn depends on reliable ROI selection and a higher signal-to-noise ratio (SNR) for better semiquantification. In concert with the ACQ-based rationale, FIN in the NIR-II window overcomes the inherent drawbacks of traditional fluorescence imaging and improves the accuracy of FIN.

The in vivo imaging quality of the NIR-I and NIR-II probes was compared. First, the anti-scattering and penetrating capability of the probes was studied by a reported capillary immersion method [55, 56]. Fluorescence was recorded after filling labeled PMs into a capillary and then immersion in a 1% Intralipid® emulsion at different depths (Fig. 4A). The boundary of the ACQ984-PM-filled capillary can be clearly outlined even at a berrying depth of 7 mm under a 1300 nm longpass filter, while that of the P2-PM-filled capillary is hardly discernable at depths greater than 3 mm (Fig. 4B). The scattering degree, displayed at a depth of 3 mm, decreases in response to the increase in the emission wavelength from 1000 nm LP to 1300 nm LP (Fig. 4B). To avoid systemic errors associated with the equipment, the ratio of the full width at half-maximum (FWHM) to the capillary length (L_c) is utilized to compare the scattering effect. With increasing penetration depth, only a slight change in the FWHM/L_c is observed for the ACQ984-based systems under 1300 and 1200 nm LP, while a more than fourfold increase is observed for the P2-based system in the NIR-I region, highlighting the superior resolution of NIR-II imaging (Fig. 4C).

High-resolution NIR-II imaging provides clear visualization of vascular systems, including both blood vessels and lymphatics. The optimal NIR-II imaging conditions were selected, with the 1300 nm LP showing the best discrimination of blood vessels (Fig. S6A&B). ACQ984-based NIR-II imaging revealed the distribution profiles of PMs in different vascular systems, e.g., the skin surface vessels, external jugular veins, and femoral arteries (Fig. 4D). Nevertheless, P2-based NIR-I imaging only exhibits intensity-relevant distribution throughout the body with a resolution too low to identify various vessels or organs (Fig. 4D). Jugular veins imaged with ACQ984 showed a narrower distribution with an FWHM of 0.35, in contrast to the 1.91 obtained with P2 (Fig. 4E). A greater SNR was also achieved for ACQ984 than for P2 (2.94 vs. 1.20) (Fig. 4F). Similarly, the femoral arteries had narrower FWHM and greater SNR (Fig. S6C and S6D). ACQ984 achieves high-resolution imaging of extremely thin blood vessels. The cross-sectional intensity distribution of the abdomen showed several sharp peaks that represent skin surface vessels, demonstrating the ability of ACQ984 to image tiny vascular structures (Fig. 4G). High-contrast imaging of vascular systems enables accurate localization and continuous online detection and thereby probable in situ real-time monitoring of pharmacokinetics (PK). The improved imaging depth of NIR-II enables the observation of deeper organ structures. Compared to NIR-I imaging, ACQ984-based imaging distinctly identifies major and branched blood vessels. Therefore, the vascular structures within various tissues, especially the mononuclear phagocytosis system (MPS), can be partially visualized due to abundant blood perfusion (Fig. 4H, left panel, yellow arrow). Even distal

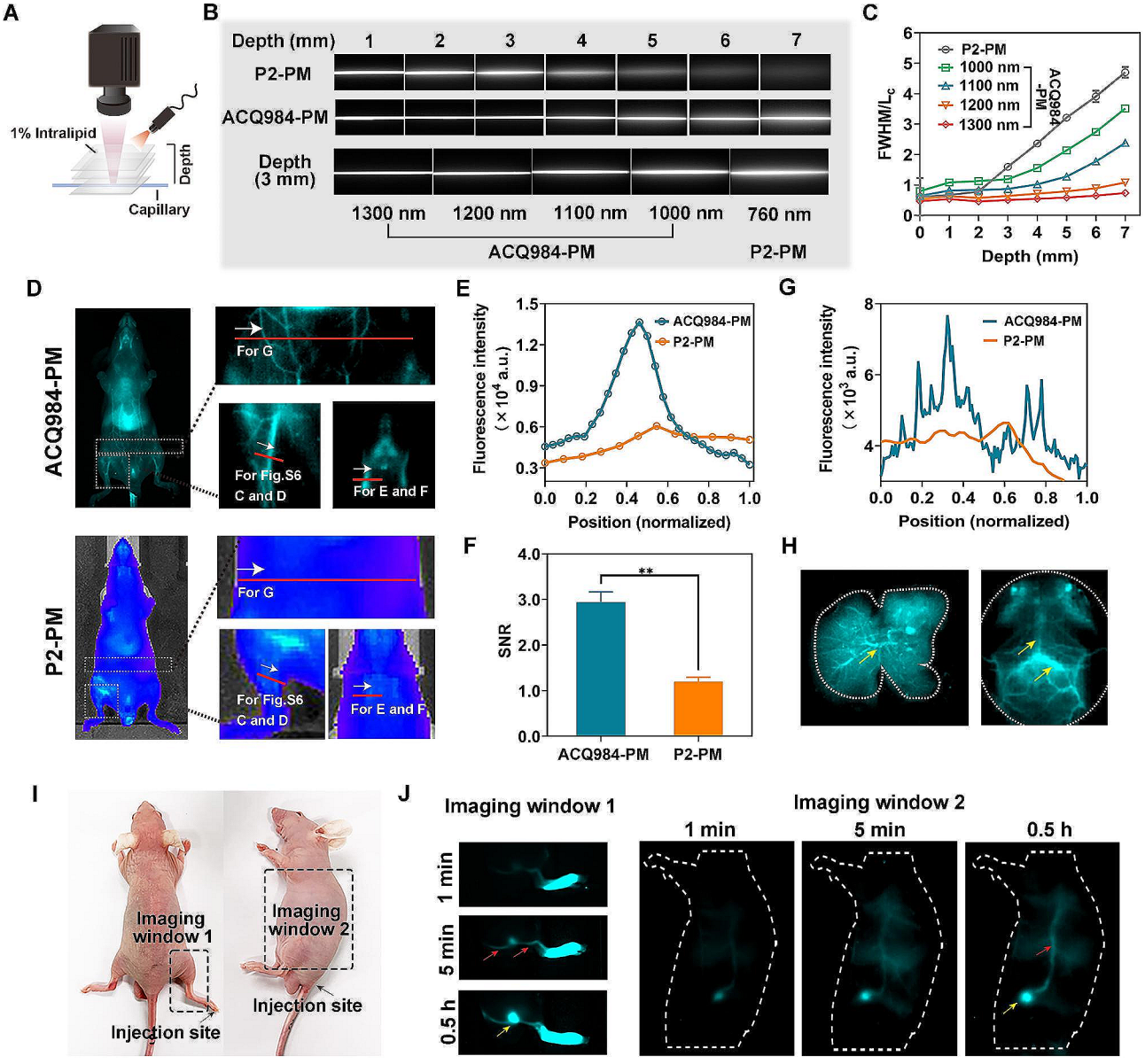

Fig. 4 ACQ984-based NIR-II imaging revealed well-defined organs and tissues. (**A**) NIR fluorescence imaging setup for the tissue phantom study. (**B**)In vitro comparison of NIR-I and NIR-II imaging (1300 nm LP) with probe-loaded capillaries immersed at different depths in a 1% Intralipid® emulsion. (**C**) FWHM curves from 1000 to 1300 nm LP for ACQ984- and P2-based imaging. (**D**) Comparison of ACQ984-based imaging and P2-based imaging for visualizing systemic vascular structures, including the external jugular veins (for **E**&**F**), femoral arteries (for Fig. S6C&D) and skin surface vessels (for **G**). (White arrows indicate the direction of the normalized position from 0 to 1.) (**E**)-(**G**) Comparison of imaging quality between ACQ984 and P2. (**E**) Fluorescence intensity profiles across the red line of interest of external jugular veins for vascular FWHM calculation. (The positions of points distributed along the red line were normalized.) (**F**) Corresponding vascular signal background ratio (SNR) analysis with intensity across the red line. ** $P < 0.01$. (**G**) Fluorescence intensity profiles across the red line of interest of skin surface vessels, distinguishing extremely thin blood vascular structures. (**H**) ACQ984-based imaging for visualization of vascular structures (yellow arrows) in multiple organs, such as the liver (left) and brain (right). (**I**) The regions (labeled with black squares; left: imaging window 1; right: imaging window 2) were imaged in nude mice to visualize the lymphatic system after the intradermal injection of ACQ984-PM into the paw (left) and tail base (right). (**J**) ACQ984-based imaging was used to visualize lymphatic nodes (yellow arrows) and lymphatic collecting vessels (red arrows). Popliteal lymph nodes were observed in imaging window 1, and inguinal lymph nodes were observed in imaging window 2

tissues, such as the brain (Fig. 4H, right panel), can be clearly visualized. The transverse (lower arrow) and sagittal sinuses (upper arrow) of the brain were also clearly imaged (Fig. 4H) [57, 58].

The lymphatic system could also be clearly visualized by NIR-II imaging. After injection in the paws and tail root, as shown in Fig. 4I, the popliteal lymph node and inguinal lymph node are clearly visible (Fig. 4J, yellow arrows) [59, 60]. Regional lymphatics (afferent and

efferent lymph vessels) and internodal collecting lymphatics became apparent with time (Fig. 4J, red arrows). After 12 h, the systemic circulation is illuminated following transport of the PMs from the lymphatics to the blood vessels (Fig. S7).

NIR-II imaging also clearly outlines the boundaries of organs such as the liver, making ROI selection more objective (Fig. S6E&F). The fluorescence decreased abruptly from the hepatic to the blank regions at 1300 nm FP, with a slope significantly greater than that of the 1000 nm FP and P2-based NIR-I imaging, reinforcing the contrast between the ROIs and non-ROIs (Fig. S6F&G). Ideally, the organ boundaries can be localized by the fluorescence descendance slope-based mathematical calculation of the ROI. An improved resolution makes ROI selection more rational. The SNR calculated from the liver region to the lower blank region at 1300 nm was significantly greater than that of P2-based imaging (2.35 vs. 1.59) (Fig. S6E). The improved SNR contributes to more accurate semiquantification.

Real-time in situ PK study and establishment of in vivo–ex vivo correlation

In view of the high imaging resolution of blood vessels, we propose that in situ real-time fluorescence monitoring could be utilized for PK analysis, avoiding tedious sampling procedures involved in traditional PK studies such as orbital blood collection and processing.

First, the correlation between fluorescence and nanocarriers was investigated. Good linearity between particles, expressed as material concentration, and fluorescence was established in blood in vitro for all three kinds of nanocarriers (Fig. S8A). Furthermore, the linearity is evaluated at different depths by employing capillary immersion protocols. Good linearity can also be observed with regression coefficients (r^2) of 0.997, 0.986, 0.972, and 0.981 at depths of 0, 2, 3, and 4 mm, respectively, after the immersion of ACQ984-PM-filled capillaries in a 1% Intralipid® emulsion (Fig. 5A&S8B). Due to the interference caused by reflection of the capillaries themselves, the detection limit increased from 0.125 mg/mL to 0.75 mg/mL. The linearity is not influenced by the immersion depth (Fig. 5A&S8B).

Having established the reliability of utilizing fluorescence to analyze nanocarriers, the PK of various nanocarriers can be studied by in vivo live imaging based on an ROI strategy (Fig. S8C for ROI selection). Figure 5B shows snapshots of the blood vessels (external jugular vein) captured at different time points after the intravenous administration of PMs. Each kind of nanocarrier showed a distinct elimination profile (Fig. 5B). In particular, rapid and continuous data acquisition within a few seconds makes it feasible to capture the C_{max} point, which is an important parameter for PK analysis, especially for fast elimination systems, and is usually very difficult to capture by manual sampling (Fig. 5C). The fluorescence readouts are displayed as normalized data by setting the signals at 2 min to 100%, which corresponds to the first collection point ex vivo (Fig. 5D). A comparison of the data acquired by live imaging and ex vivo blood sampling at corresponding time points (2, 5, 15, 30, 60, and 120 min) confirmed the establishment of an in vivo-ex vivo correlation. ACQ984-PMs exhibited relatively stable fluorescence within 2 h, fluctuating within the 90–100% range both in vivo and ex vivo (Fig. 5D). No significant differences were observed between the in vivo and ex vivo data (Fig. 5E). For the fast-eliminating ACQ984-PCL and ACQ984-PEG-PCL nanoparticles, a good correlation was also established between the in vivo and ex vivo data. The ACQ984-PEG-PCL nanoparticles exhibited a strong linear correlation with Pearson's $R=0.96$ and $r^2=0.91$ (Fig. 5E). Although PCL nanoparticles undergo extraordinarily fast blood elimination, they still correlated well ($R=0.95$) and showed an acceptable fit of 0.90 (Fig. 5E).

Blood PK parameters are calculated by both statistical moment and compartmental approaches. PK analysis requires enough time points to display different disposition phases. PMs are not included for calculation because their elimination phases cannot be detected due to the short sampling time limited by animal anesthesia. Notably, the parameters calculated here are relative values based on semiquantification. For the ACQ984-PCL nanoparticles, no significant differences were observed between the in vivo and ex vivo data for MRT_{0-t} and AUC_{0-t} (Table S3). For the ACQ984-PEG-PCL nanoparticles, the values of MRT_{0-t} also showed nonsignificant differences. However, due to the bias caused by fluctuations in the fluorescence value, differences existed for the AUC_{0-t} (54.3±5.2 vs. 78.2±7.0) (Table S3). Both in vivo and ex vivo data are perfectly fitted to a two-compartment model. Although the inevitable bias between in vivo and ex vivo curves makes hybrid parameter prediction difficult, important basic parameters such as $t_{1/2\alpha}$, $t_{1/2\beta}$, *AUC*, and *CL* can partially correspond, some of which exhibit no significant differences (Table S4).

Biodistribution and hepatic/splenic PK

The in vivo biodistribution of different types of nanoparticles was investigated with the newly established imaging tool. After entering systemic circulation, most nanocarriers are captured by MPS organs such as the liver and spleen. Their high fluorescence accumulation makes it feasible for robust online detection to realize good in vivo-ex vivo correlation. $mPEG_{2k}$-$PDLLA_{2k}$ micelles (PMs), which are small and decorated with PEG, have long circulation times, as visualized by the fluorescence remaining in blood vessels for more than 12 h (Fig. 6A, S9A&B). A decrease in the number of

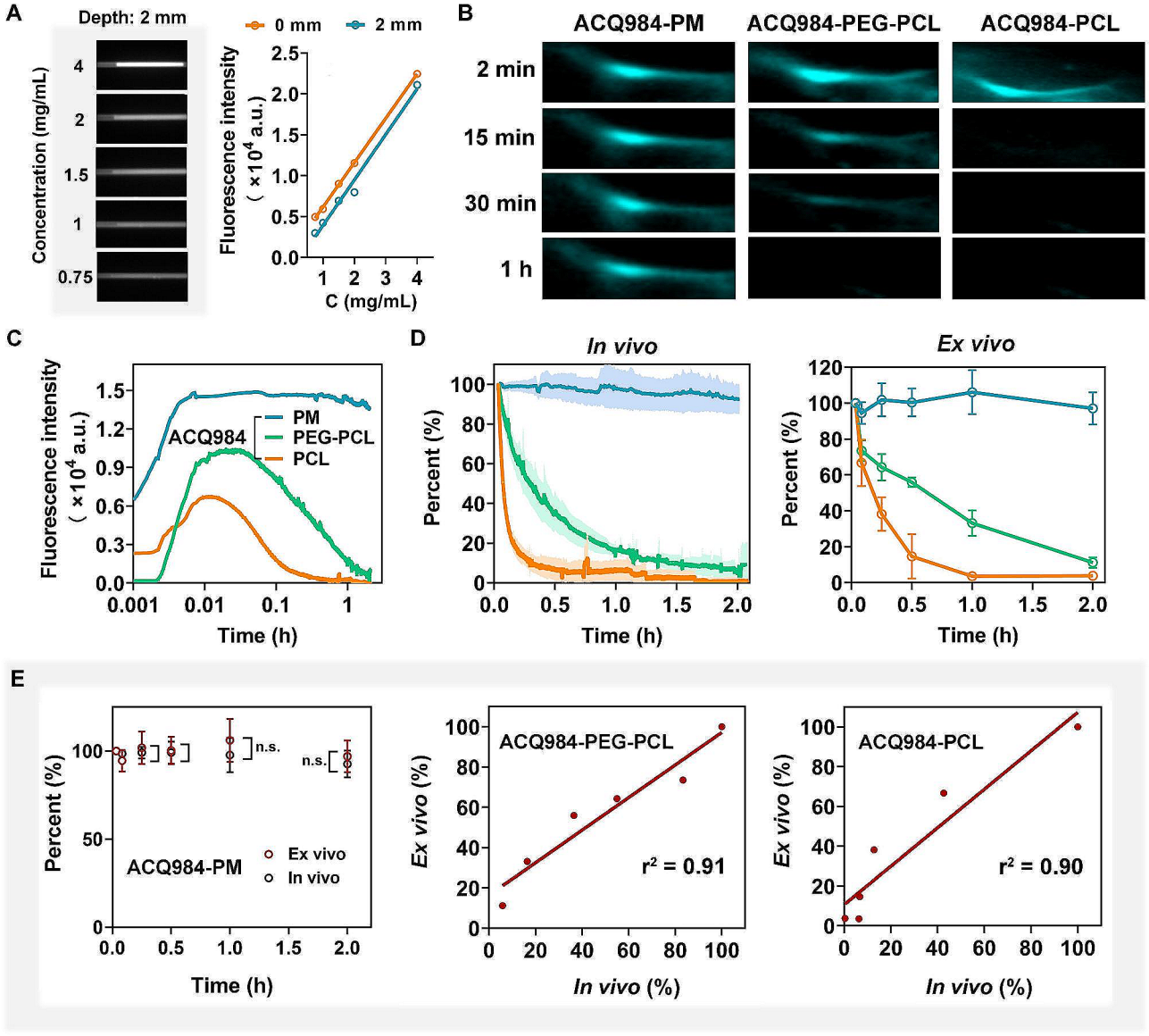

Fig. 5 ACQ984-based NIR II imaging realized good linear correlation betweenin vivo and ex vivo blood pharmacokinetics. (**A**) Fluorescence images of capillaries filled with different concentrations of ACQ984-PM dispersions at a 2 mm depth; linear relationship between particle concentration and fluorescence intensity at a certain depth. For the immersion capillaries filled with different concentrations of ACQ984-PM dispersions in 1% Intralipid®, the fluorescence intensity was calculated by subtracting the background of the blank capillary. (**B**) Online detection of changes in the blood fluorescence intensity of the ACQ984-PM, ACQ984-PEG-PCL and ACQ984-PCL nanoparticles. (**C**) Changes in the fluorescence intensity of the ACQ984-PM, ACQ984-PEG-PCL and ACQ984-PCL nanoparticles in the blood after perfusion to equilibrium and elimination. ($n=3$ for the PM group; $n=4$ for the ACQ984-PEG-PCL and ACQ984-PCL groups; the SDs are provided in Data Sheet 1.) (**D**) Blood fluorescence intensity changes (expressed as percentages) of ACQ984-PM, ACQ984-PEG-PCL and ACQ984-PCL in vivo and ex vivo. For in vivo imaging, the first time point (2 min) was selected to be the same as that for in vitro blood collection. (**E**) In vivo and ex vivo correlation of the blood pharmacokinetics of ACQ984-PM, ACQ984-PEG-PCL and ACQ984-PCL. For ACQ984-PM, each point was compared to test whether a significant difference existed between the in vivo and ex vivo results. n.s.: nonsignificant

blood vessel particles is accompanied by corresponding hepatic enrichment. As the main distribution organ, the liver exhibited maximum fluorescence at 8 h, which sustained for more than 12 h (Fig. 6B). Fluorescence with a well-defined image shape appears in the gastrointestinal tract, suggesting that bile excretion from intact particles is a potential elimination pathway for PMs (Fig. S9D). The hepatic fluorescence slowly decreased from 12 h to 48 h, as shown in Figure S9E, indicating metabolism by the hepatic tissue. In vivo imaging further revealed particle transport to peripheral compartments, with the skin being gradually illuminated after 8 h (Fig. S9A). Further ex vivo inspection of skin tissues revealed this peripheral distribution for as long as 24 h (Fig. S9C). Unlike the ACQ984-PMs, the ACQ984-PCL and ACQ984-PEG-PCL nanoparticles showed faster blood elimination.

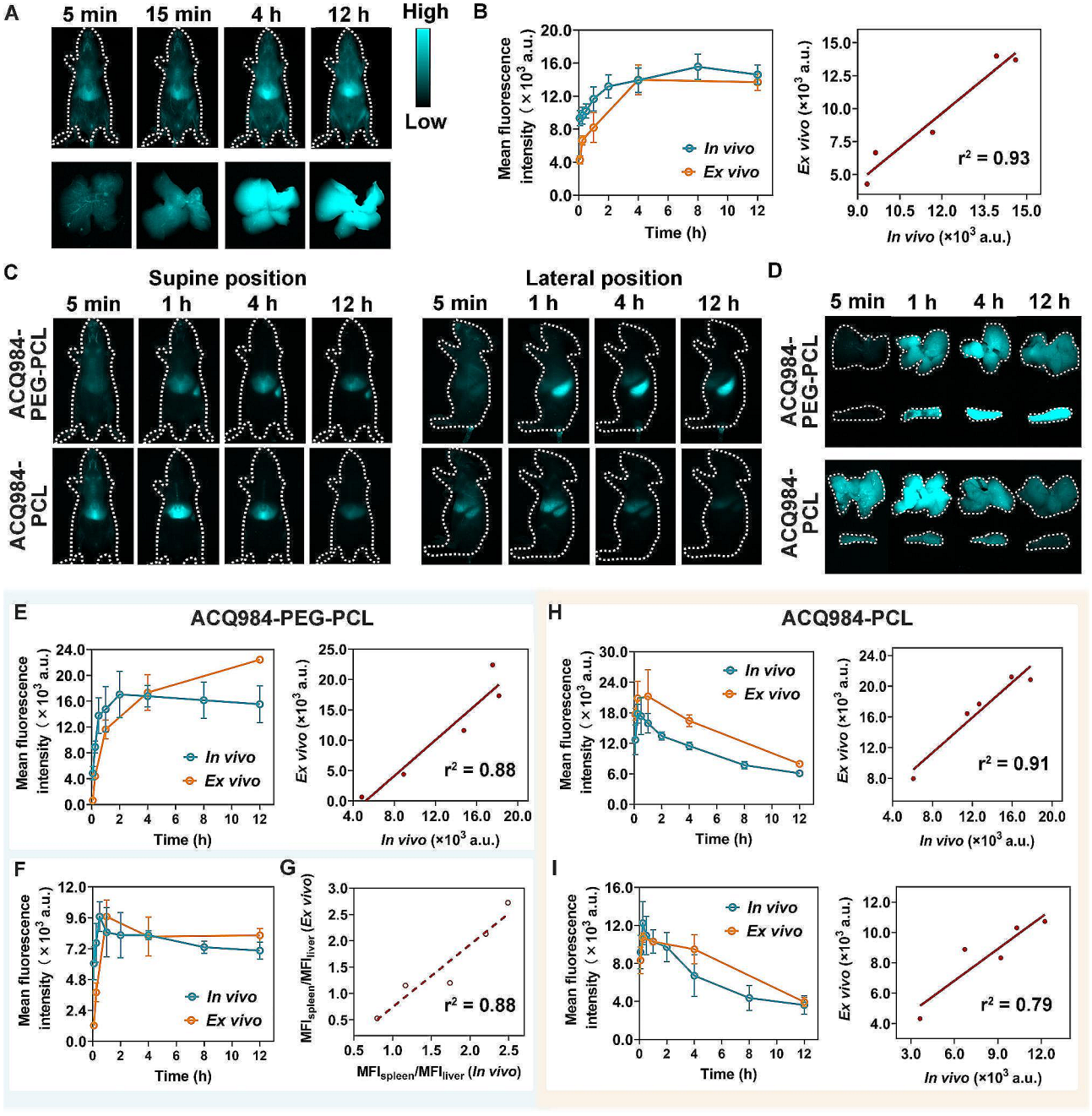

Fig. 6 ACQ984-based imaging results in good in vivo-in vitro correlation of MPS organs. (**A**) In vivo and ex vivo imaging of the hepatic biodistribution of ACQ984-PMs. (**B**) Profiles of the mean fluorescence intensity of ACQ984-PMs in the liver both in vivo ($n = 3$) and ex vivo ($n = 3$) and the corresponding linear correlation results. (**C**) Live and (**D**) ex vivo (liver and spleen) imaging of the biodistribution of the ACQ984-PEG-PCL and ACQ984-PCL nanoparticles. (**E**) Profiles of changes in the mean fluorescence intensity of ACQ984-PEG-PCL in the spleen between in vivo ($n = 3$) and ex vivo ($n = 3$) conditions and the corresponding correlations. (**F**) Changes in the mean fluorescence intensity of ACQ984-PEG-PCL in the liver between in vivo ($n = 3$) and ex vivo ($n = 3$) conditions. (**G**) Distribution proportion correlation between in vivo and ex vivo data. The distribution proportion was calculated as the mean fluorescence intensity ratio between the spleen (MFI_{spleen}) and liver (MFI_{liver}) at each selected time. The high correlation of the distribution proportion made accurate predictions of targeting efficiency if the spleen was assumed to be the targeting tissue and the liver was assumed to be the nontarget tissue. The targeting efficiency was calculated as the ratio of the AUC of the $_{spleen}$/AUC of the $_{liver}$. (**H**) (**I**) Changes in the mean fluorescence intensity of ACQ984-PCL in the liver and spleen in vivo ($n = 3$) and ex vivo ($n = 3$) and the corresponding correlations

ACQ984-PEG-PCL nanoparticles were more prone to accumulation in the spleen and were even retained for several days (Fig. 6C, D&S9F-H). The ACQ984-PCL nanoparticles showed stronger fluorescence intensity in the liver but exhibited increased fluorescence within 30 min to 1 h, after which they were rapidly eliminated in the spleen (Fig. 6C and D, S9I & S9J). The in vivo behaviors of the three types of nanoparticles correspond to their own properties. PMs with a small size and dense PEG coverage could avoid capture by the MPS and be retained in blood for a long time. They can pass through the space between liver sinusoidal endothelial cells and mainly accumulate in the liver due to the high tissue blood supply. PCL nanoparticles, which are much larger and have highly hydrophobic surfaces, are prone to opsonization by complement proteins and capturing by macrophages located in organs of the MPS, especially the liver, resulting in rapid blood elimination and rapid liver accumulation. PEG-PCL nanoparticles with partial PEG coverage showed a moderate in vivo elimination rate. Compared to that of the PCL nanoparticles, the longer blood circulation time of the mPEG-PCL nanoparticles may increase the likelihood of accessing MPS organs other than the liver, such as the spleen. The fact that PEGylation aids in hepatic evasion but facilitates splenic trapping was consistent with earlier findings [61].

The distribution behaviors of nanocarriers are commonly demonstrated by fluorescence imaging of ex vivo tissues with semiquantification. The current study tests the plausibility of in vivo imaging of nanocarrier distribution and in situ real-time PK analysis. For ACQ984-PMs, the semiquantified in vivo fluorescence of hepatic tissues changed almost in parallel with that of ex vivo tissues, showing good correlation with Pearson's $R=0.97$ and a strong linear fit with $r^2=0.93$ (Fig. 6B). For ACQ984-PEG-PCL, the major accumulating organ, the spleen, also showed good in vivo-ex vivo correlation, with Pearson's $R=0.95$ and $r^2=0.88$ (Fig. 6E). Assuming that the spleen is the target organ, the ratio between the target and non-targeting organs, such as the liver, exhibited good in vivo-ex vivo correlation, with a high Pearson's R of 0.95 and a r^2 of 0.88 (Fig. 6G). The targeting efficiencies calculated ex vivo or in vivo were not significantly different (1.91 ± 0.49 vs. 1.81 ± 0.29), which makes this method promising for direct in vivo prediction of tissue targeting efficiency. Although the large fluctuation in hepatic fluorescence caused by individual animals makes it difficult to establish linearity, a strong in vivo-ex vivo correlation could still be achieved with Pearson's $R=0.79$ (Fig. 6F). The ACQ984-PCL nanoparticles also exhibited good correlation in both the liver and spleen. In the liver, Pearson's R and the r^2 reached 0.96 and 0.91, respectively (Fig. 6H). In the spleen, Pearson's R and the r^2 also reached 0.91 and 0.79, respectively (Fig. 6I).

These results support the idea that ACQ984-based NIR-II imaging reflects or even allows direct in vivo semiquantification of the particle distribution in major organs, such as the liver and spleen, making it a promising tool for FIN in vivo. Due to the high spatial resolution of ACQ984-based NIR-II imaging, in vivo detection and real-time semiquantification have become more accessible and accurate. Compared to traditional ex vivo sampling, this non-invasive online detection method may be more promising for PK analysis.

Taken together, the newly developed NIR-II fluorophore demonstrate more favorable features than other selected probes for FIN, which are summarized in Table S5.

Conclusions

In summary, the BODIPY-structured NIR-II ACQ probe ACQ984 was synthesized for in vivo nanoparticle tracking. Compared to other selected fluorescence probes, ACQ984 has NIR-II emission, better ACQ effects, and excellent fluorescence stability. More importantly, ACQ984 exhibited the lowest reillumination in the complex endogenous environment. Although ACQ984 can be efficiently loaded into polymeric micelles and nanoparticles, IR-1061, which has a comparable ACQ effect, is too sensitive to environmental changes to efficiently label nanocarriers, especially under physiological conditions. Following intravenous administration of the ACQ984-labeled nanocarriers, the main organs and vascular systems were clearly outlined by an IVIS system. In contrast, labeling by the NIR-I probe P2 only results in intensity-relevant fluorescence but not intricate microstructures of the vascular system. ACQ984-based NIR-II imaging has good in vivo-ex vivo correlation with blood pharmacokinetics and fluorescence accumulation in the main organs of the MPS. It is concluded that the NIR-II and ACQ features of the newly developed fluorophores enable in vivo tracking and analysis of nanocarriers with higher resolution and enhanced accuracy.

Supplementary Information

The online version contains supplementary material available at https://doi.org/10.1186/s12951-024-02761-5.

Supplementary Material 1

Author contributions

Z.Z. and C.L. performed the experiments; Z.Z., Y.L., and H.H. analyzed the data; W.W. Z.C., W.Z., and Q.Z supervised the project; Z.Z., C.L., H.H., and W.W. wrote the manuscript. All of the authors have read and approved the final manuscript.

Funding

This work was financially supported by the National Natural Science Foundation of China (82273867 and 82030107) and the Science and Technology Commission of Shanghai Municipality (21430760800).

Data availability
Data will be made available on request.

Declarations

Ethics approval and consent to participate
The animal experiments were approved by the Institutional Animal Care and Use Committee at the School of Pharmacy, Fudan University (No. 2022-08-YJ-WW-90).

Consent for publication
Not applicable.

Competing interests
The authors declare no competing interests.

Received: 8 March 2024 / Accepted: 6 August 2024
Published online: 14 August 2024

References

1. Puri S, Mazza M, Roy G, England RM, Zhou L, Nourian S, et al. Evolution of Nanomedicine formulations for targeted delivery and controlled release. Adv Drug Deliv Rev. 2023;200:114962.
2. Shan X, Gong X, Li J, Wen JY, Li Y, Zhang Z. Current approaches of nanomedicines in the market and various stage of clinical translation. Acta Pharm Sin B. 2022;12:3028–48.
3. Liu Q, Zou J, Chen Z, He W, Wu W. Current research trends of nanomedicines. Acta Pharm Sin B. 2023;13:4391–416.
4. Wu W, Li T. Unraveling the in vivo fate and cellular pharmacokinetics of drug nanocarriers. Adv Drug Deliv Rev. 2019;143:1–2.
5. Mahmoudi M. Debugging Nano-Bio interfaces: systematic strategies to accelerate clinical translation of nanotechnologies. Trends Biotechnol. 2018;36:755–69.
6. Cao M, Zhang K, Zhang S, Wang Y, Chen C. Advanced Light Source Analytical techniques for exploring the Biological Behavior and Fate of Nanomedicines. ACS Cent Sci. 2022;8:1063–80.
7. Wu W, Li T. Deepening the understanding of the in vivo and cellular fate of nanocarriers. Adv Drug Deliv Rev. 2022;189:114529.
8. Roy S, Bag N, Bardhan S, Hasan I, Guo B. Recent progress in NIR-II fluorescence imaging-guided drug delivery for cancer theranostics. Adv Drug Deliv Rev. 2023;197:114821.
9. Vargas-Nadal G, Kober M, Nsamela A, Terenziani F, Sissa C, Pescina S, et al. Fluorescent multifunctional Organic nanoparticles for Drug Delivery and Bioimaging: a Tutorial Review. Pharmaceutics. 2022;14:2498.
10. Li P, Wang D, Hu J, Yang X. The role of imaging in targeted delivery of nanomedicine for cancer therapy. Adv Drug Deliv Rev. 2022;189:114447.
11. Lebreton V, Legeay S, Saulnier P, Lagarce F. Specificity of pharmacokinetic modeling of nanomedicines. Drug Discov Today. 2021;26:2259–68.
12. Hu X, Dong X, Lu Y, Qi J, Zhao W, Wu W. Bioimaging of nanoparticles:the crucial role of discriminating nanoparticles from free probes. Drug Discov Today. 2017;22:382–7.
13. Hollis CP, Weiss HL, Leggas M, Evers BM, Gemeinhart RA, Li T. Biodistribution and bioimaging studies of hybrid paclitaxel nanocrystals: lessons learned of the EPR effect and image-guided drug delivery. J Control Release. 2013;172:12–21.
14. Hollis CP, Weiss HL, Evers BM, Gemeinhart RA, Li T. In vivo investigation of Hybrid Paclitaxel nanocrystals with dual fluorescent probes for Cancer Theranostics. Pharm Res. 2014;31:1450–9.
15. Yang Y, Xie Y, Zhang F. Second near-infrared window fluorescence nanoprobes for deep-tissue in vivo multiplexed bioimaging. Adv Drug Deliv Rev. 2023;193:114697.
16. Feliu N, Docter D, Heine M, del Pino P, Ashraf S, Kolosnjaj-Tabi J, et al. In vivo degeneration and the fate of inorganic nanoparticles. Chem Soc Rev. 2016;45:2440–57.
17. Qi J, Hu X, Dong X, Lu Y, Lu H, Zhao W, et al. Towards more accurate bioimaging of drug nanocarriers: turning aggregation-caused quenching into a useful tool. Adv Drug Deliv Rev. 2019;143:206–25.
18. Zhang H, Li H, Cao Z, Du J, Yan L, Wang J. Investigation of the in vivo integrity of polymeric micelles via large Stokes shift fluorophore-based FRET. J Control Release. 2020;324:47–54.
19. Wolf MP, Liu K, Horn TFW, Hunziker P. FRET in a polymeric nanocarrier: IR-780 and IR-780-PDMS. Biomacromolecules. 2019;20:4065–74.
20. Chen T, He B, Tao J, He Y, Deng H, Wang X, et al. Application of Forster Resonance Energy Transfer (FRET) technique to elucidate intracellular and in vivo biofate of nanomedicines. Adv Drug Deliv Rev. 2019;143:177–205.
21. Sun X, Wang G, Zhang H, Hu S, Liu X, Tang J, et al. The blood clearance kinetics and pathway of polymeric micelles in Cancer Drug Delivery. ACS Nano. 2018;12:6179–92.
22. Li D, Zhuang J, Yang Y, Wang D, Yang J, He H, et al. Loss of integrity of doxorubicin liposomes during transcellular transportation evidenced by fluorescence resonance energy transfer effect. Colloids Surf B. 2018;171:224–32.
23. Cayre F, Mura S, Andreiuk B, Sobot D, Gouazou S, Desmaele D, et al. In vivo FRET imaging to predict the risk Associated with hepatic Accumulation of Squalene-based Prodrug nanoparticles. Adv Healthc Mater. 2018;7:1700830.
24. Geissler D, Hildebrandt N. Recent developments in Forster resonance energy transfer (FRET) diagnostics using quantum dots. Anal Bioanal Chem. 2016;408:4475–83.
25. Goryacheva OA, Beloglazova NV, Vostrikova AM, Pozharov MV, Sobolev AM, Goryacheva IY. Lanthanide-to-quantum dot Forster resonance energy transfer (FRET): application for immunoassay. Talanta. 2017;164:377–85.
26. Smith JT, Sinsuebphon N, Rudkouskaya A, Michalet X, Intes X, Barroso M. In vivo quantitative FRET small animal imaging: intensity versus lifetime-based FRET. Biophys Rep (N Y). 2023;3:100110.
27. Lebreton V, Kaeokhamloed N, Vasylaki A, Hilairet G, Mellinger A, Bejaud J, et al. Pharmacokinetics of intact lipid nanocapsules using new quantitative FRET technique. J Control Release. 2022;351:681–91.
28. Huanga X, Song J, Yung B, Huang X, Xiong Y, Chen X. Ratiometric optical nanoprobes enable accurate molecular detection and imaging. Chem Soc Rev. 2018;47:2873–920.
29. Li C, Chen G, Zhang Y, Wu F, Wang Q. Advanced fluorescence Imaging Technology in the Near-Infrared-II window for Biomedical Applications. J Am Chem Soc. 2020;142:14789–804.
30. Wang Y, Zhang Y, Wang J, Liang X. Aggregation-induced emission (AIE) fluorophores as imaging tools to trace the biological fate of nano-based drug delivery systems. Adv Drug Deliver Rev. 2019;143:161–76.
31. Li T, Cao K, Yang X, Liu Y, Wang X, Wu F. An oral ratiometric NIR-II fluorescent probe for reliable monitoring of gastrointestinal diseases in vivo. Biomaterials. 2023;293:121956.
32. Hu X, Zhang J, Yu Z, Xie Y, He H, Qi J, et al. Environment-responsive aza-BODIPY dyes quenching in water as potential probes to visualize the in vivo fate of lipid-based nanocarriers. Nanomedicine. 2015;11:1939–48.
33. He H, Wang L, Ma Y, Yang Y, Lv Y, Zhang Z, et al. The biological fate of orally administered mPEG-PDLLA polymeric micelles. J Control Release. 2020;327:725–36.
34. Zoya I, He H, Wang L, Qi J, Lu Y, Wu W. The intragastrointestinal fate of paclitaxel-loaded micelles: implications on oral drug delivery. Chin Chem Lett. 2021;32:1545–9.
35. Fu Y, Shi C, Li X, Wen T, Wu Q, Zhang A, et al. Demonstrating Biological Fate of nanoparticle-loaded dissolving microneedles with aggregation-caused quenching probes: influence of Application sites. Pharmaceutics. 2023;15:169.
36. Huang Z, Huang Y, Wang W, Fu F, Wang W, Dang S, et al. Relationship between particle size and lung retention time of intact solid lipid nanoparticle suspensions after pulmonary delivery. J Control Release. 2020;325:206–22.
37. Shen B, Shen C, Zhu W, Yuan H. The contribution of absorption of integral nanocrystals to enhancement of oral bioavailability of quercetin. Acta Pharm Sin B. 2021;11:978–88.
38. Cai Y, Ji X, Zhang Y, Liu C, Zhang Z, Lv Y, et al. Near-infrared fluorophores with absolute aggregation-caused quenching and negligible fluorescence re-illumination for in vivo bioimaging of nanocarriers. Aggregate. 2023;4:e277.
39. He H, Liu C, Ming J, Lv Y, Qi J, Lu Y, et al. Accurate and sensitive probing of onset of micellization based on absolute aggregation-caused quenching effect. Aggregate. 2022;3:e163.
40. Li L, Chunta S, Zheng X, He H, Wu W, Lu Y. β-Lactoglobulin stabilized lipid nanoparticles enhance oral absorption of insulin by slowing down lipolysis. Chin Chem Lett. 2024;35(4):108662.
41. Zheng X, Fang Z, Huang W, Qi J, Dong X, Zhao W, et al. Ionic co-aggregates (ICAs) based oral drug delivery: solubilization and permeability improvement. Acta Pharm Sin B. 2022;12:3972–85.

42. Fan W, Peng H, Yu Z, Wang L, He H, Ma Y, et al. The long-circulating effect of pegylated nanoparticles revisited via simultaneous monitoring of both the drug payloads and nanocarriers. Acta Pharm Sin B. 2022;12:2479–93.
43. Umezawa M, Haruki M, Yoshida M, Kamimura M, Soga K. Effects of Processing pH on Emission Intensity of Over-1000 nm Near-Infrared fluorescence of Dye-Loaded Polymer Micelle with Polystyrene Core. Anal Sci. 2021;37:485–90.
44. Bai L, Sun P, Liu Y, Zhang H, Hu W, Zhang W, et al. Novel aza-BODIPY based small molecular NIR-II fluorophores for in vivo imaging. Chem Comm (Camb). 2019;55:10920–3.
45. Zhai D, Xu W, Zhang L, Chang YT. The role of disaggregation" in optical probe development. Chem Soc Rev. 2014;43:2402–11.
46. Ueya Y, Umezawa M, Takamoto E, Yoshida M, Kobayashi H, Kamimura M, et al. Designing highly emissive over-1000 nm near-infrared fluorescent dye-loaded polystyrene-based nanoparticles for in vivo deep imaging. RSC Adv. 2021;11:18930–7.
47. Descalzo AB, Ashokkumar P, Shen Z, Rurack K. On the aggregation Behaviour and Spectroscopic properties of Alkylated and Annelated Boron-Dipyrromethene (BODIPY) dyes in aqueous solution. ChemPhotoChem. 2020;4:120–31.
48. Yeroslavsky G, Umezawa M, Okubo K, Nigoghossian K, Thi Kim Dung D, Miyata K, et al. Stabilization of indocyanine green dye in polymeric micelles for NIR-II fluorescence imaging and cancer treatment. Biomater Sci. 2020;8:2245–54.
49. Yang Q, Hu Z, Zhu S, Ma R, Ma H, Ma Z, et al. Donor Engineering for NIR-II Molecular fluorophores with enhanced fluorescent performance. J Am Chem Soc. 2018;140:1715–24.
50. Rajagopalan R, Uetrecht P, Bugaj J, Achilefu S, Dorshow R. Stabilization of the Optical Tracer Agent Indocyanine Green UsingNoncovalent interactions. Photochem Photobiol. 2000;71:347–50.
51. Bhattacharyya S, Paramanik B, Patra A. Energy Transfer and confined motion of dyes trapped in semiconducting conjugated polymer nanoparticles. J Phys Chem C. 2011;115:20832–9.
52. Ichihashi K, Umezawa M, Ueya Y, Okubo K, Takamoto E, Matsuda T, et al. Effect of the enantiomeric structure of hydrophobic polymers on the encapsulation properties of a second near infrared (NIR-II) fluorescent dye for in vivo deep imaging. RSC Adv. 2022;12:1310–8.
53. Yamamoto Y, Yasugi K, Harada A, Nagasaki Y, Kataoka K. Temperature-related change in the properties relevant to drug delivery of poly(ethylene glycol)-poly(D,L-lactide) block copolymer micelles in aqueous milieu. J Control Release. 2002;82:359–71.
54. Demirel AL, Yurteri S, Cianga I, Yagci Y. Layered morphology of poly(phenylene)s in thin films induced by substitution of well-defined poly(epsilon-caprolactone) side chains. Macromolecules. 2005;38:6402–10.
55. Li B, Lu L, Zhao M, Lei Z, Zhang F. An efficient 1064 nm NIR-II excitation fluorescent molecular dye for deep-tissue high-resolution dynamic bioimaging. Angew Chem Int Ed. 2018;57:7483–7.
56. Wu D, Xue D, Zhou J, Wang Y, Feng Z, Xu J, et al. Extrahepatic cholangiography in near-infrared II window with the clinically approved fluorescence agent indocyanine green: a promising imaging technology for intraoperative diagnosis. Theranostics. 2020;10:3636–51.
57. Bhavane R, Starosolski Z, Stupin I, Ghaghada KB, Annapragada A. NIR-II fluorescence imaging using indocyanine green nanoparticles. Sci Rep. 2018;8:115–29.
58. Liu Y, Liu J, Chen D, Wang X, Zhang Z, Yang Y, et al. Fluorination enhances NIR-II fluorescence of polymer dots for quantitative brain Tumor Imaging. Angew Chem Int Ed. 2020;59:21049–57.
59. Antaris AL, Chen H, Cheng K, Sun Y, Hong G, Qu C, et al. A small-molecule dye for NIR-II imaging. Nat Mater. 2016;15:235–42.
60. Wang S, Fan Y, Li D, Sun C, Lei Z, Lu L, et al. Anti-quenching NIR-II molecular fluorophores for in vivo high-contrast imaging and pH sensing. Nat Commun. 2019;10:1058.
61. He H, Jiang S, Xie Y, Lu Y, Qi J, Dong X, et al. Reassessment of long circulation via monitoring of integral polymeric nanoparticles justifies a more accurate understanding. Nanoscale Horiz. 2018;3:397–407.

Publisher's Note